Numerical simulation study on the interaction between hydrogen flame and particle flame in scramjet

Junjie Li [1], Suofeng Han,[1] Wenxue Han,[1] Ronggang Wei,[1] Chunbo Hu,[1] and Chao Li[2]

[1]*National Key Laboratory of Solid Rocket Propulsion, Northwestern Polytechnical University, Xi'an, Shaanxi 710072, People's Republic of China*

[2]*Unmanned System Research Institute, Northwestern Polytechnical University, Xi'an, Shaanxi 710072, People's Republic of China*

Research on scramjet engines using hydrogen as fuel has achieved significant progress. To further enhance the performance of scramjet engines, the concept of using composite fuels comprising high-density powder fuel and hydrogen has been proposed. Current research focuses primarily on how hydrogen flames facilitate the heat release of powder fuels, but there has been limited investigation into the effects of powder injection on hydrogen flame flow-field parameters. Addressing this issue, numerical simulation methods are employed to optimize the hydrogen injection strategy in a two-stage cavity scramjet engine. Subsequently, the study focuses on the influence of particle injection expansion angle (0°, 15°, 30°, 45°) and particle injection swirl (0, 0.2, 0.3, 0.4) on hydrogen flame flow-field parameters. The computational results indicate that when the hydrogen injection flow rate is 1 g/s in both stages of the cavity, the hydrogen flame flow field exhibits higher temperature and Mach numbers. Expanding the particle injection expansion angle and increasing the particle injection swirl can enhance the combustion efficiency of boron particle. Injecting powder fuel into the aforementioned hydrogen flame flow field leads to a decrease in flame flow-field temperature.

I. INTRODUCTION

Scramjet utilizes oxygen from the atmosphere as an oxidizer. Compared to traditional rocket and turbojet engines, scramjet engines possess advantages such as lightweight construction, simple structure, and the ability to achieve sustained supersonic flight. They enable supersonic flight within the atmosphere and across atmospheric boundaries, making them a crucial component of future aerospace propulsion systems, garnering significant attention from nations worldwide [1,2].

Hydrogen, with its high calorific value, excellent ignition and combustion characteristics, and nonpolluting combustion products, has emerged as the ideal fuel for scramjets [3]. Extensive research has been conducted on the application of hydrogen fuel in scramjet, including studies on the combustion reaction mechanisms of hydrogen and oxygen under supersonic airflow conditions [4,5], as well as strategies for enhancing hydrogen-oxygen flame combustion [6,7].

In scramjets, common combustion enhancement strategies include struts [8–10], tower bridges [11–13], and cavities [14–16]. Among these, cavities have attracted significant research attention and application due to their simple construction, high mixing efficiency, and minimal total pressure loss [17,18]. To further improve mixing combustion efficiency, the concept of "multiple cavities" has been proposed. Numerous research findings indicate that scramjets employing multiple cavities can achieve efficient combustion [19,20]. However, considering the impact of cavities on total pressure loss in supersonic airflow, scramjets often adopt a dual-cavity structure [21–23]. Apart from flame-holding structures, the influence of injection strategies on fuel ignition and combustion

characteristics has been studied. In addition to injection position and flow rate, significant progress has been made in research related to the fuel injection expansion angle [24] and swirl degree [25,26] of fuel injection.

Although hydrogen is favored for use in scramjets, challenges such as its low density at standard pressure and temperature, as well as issues related to safe storage and transportation, limit its practical application [3]. Currently, there are two technological approaches to address these issues. One involves substituting a portion of the hydrogen with high-density fuels, such as solid powder fuels [27,28]. In [28], the ignition and combustion characteristics of boron particles in supersonic airflow were studied. However, according to the calculation results, ignition of the particles only occurs at positions far from the injection point. The other approach entails using metal hydride fuels to address the storage and transportation challenges associated with hydrogen [29,30]. Both of these approaches leverage the higher energy density of powder fuels, their nondisruptive combustion products, and the advantages of simpler fuel delivery system structures and convenient storage and maintenance [31]. Among common powder fuels, boron stands out due to its high heat value and nontoxic combustion products, making it particularly suitable as a propellant for powder fuel scramjets. However, ignition and combustion of boron powder require a process involving endothermic heating and rupture of surface oxide layers, resulting in longer ignition delays [32]. In scramjets, the essence of the hydrogen/boron powder fuel flame involves injecting boron particles into the hydrogen combustion flame field.

Current research focuses primarily on improving the combustion efficiency of powder fuels in supersonic airflow, but there has been limited study on the effects of powder fuel injection on the hydrogen combustion flame field. This paper focuses on the combustion chamber of a dual-cavity scramjet, studying the effects of boron powder fuel injection expansion angle and swirl degree on the combustion efficiency of powder fuels and the parameters of the hydrogen combustion flame field.

II. NUMERICAL METHODOLOGY

This paper adopts the same numerical methodology as that in Ref. [28], The detailed numerical method and verification process will not be described in this paper. The following only shows the numerical model and model verification results required for subsequent analysis:

A. Gas phase governing equation

The governing equations for the gas phase in supersonic flow are represented by a set of N-S control equations, which include mass, momentum, energy, and species equations. The specific equation is shown in the following formula [27]:

The mass equation:

$$\nabla \cdot (\alpha \rho_g U_g) = S_m. \tag{1}$$

The momentum equation:

$$\nabla \cdot (\alpha \rho_g \mathbf{U_g} \mathbf{U_g}) = -\alpha \nabla p + \nabla \cdot (\alpha \tau_{eff}) + \alpha \rho_g \mathbf{g} + S_U. \tag{2}$$

The energy equation:

$$\nabla \cdot [\alpha \mathbf{U}_g \rho_g (h + K)] - \nabla \cdot (\alpha \alpha_{eff} \nabla h) = \alpha \nabla p + \alpha \rho_g \mathbf{U}_g \cdot g + Q + S_h. \tag{3}$$

The species equation:

$$\nabla \cdot (\alpha \rho_g \mathbf{U}_g Y_i) = \nabla \cdot (\alpha D_{i,\,eff} \nabla[\rho_g Y_i]) + S_i + S_{R_i} \tag{4}$$

where α, ρ_g, $\mathbf{U}_g$, and p are the volume fraction of the gas phase or the porosity, density, velocity, and pressure. The right-hand side terms S_m, S_U, S_h, and S_i are the source terms and describe the two-way coupling of mass, momentum, energy, and species, respectively. Q and S_{R_i} are the reaction

heat and species source terms, respectively, due to the reactions. The effective stress tensor (τ_{eff}) is the sum of the viscous and turbulent stress. The effective dynamic thermal diffusivity α_{eff} and mass diffusion coefficient for species D_{eff} also take both the viscous and turbulent contributions into account.

For the turbulence model, this paper selects the two-equation k-ω shear stress transport (SST) turbulence model proposed by Menter [33]. This model has been widely used in the numerical simulation of supersonic flow [34,35]. The principle of the calculation is to consider flow with shear at a low Reynolds number at the near wall and to neglect turbulent viscosity at the far wall.

B. Particle phase governing equation

The random orbital model in the particle orbital model is chosen, and the dynamics of the particles can be characterized by the following equation [36]:

$$\frac{\mathrm{d}\vec{X}_{\text{p}}}{\mathrm{d}t} = \vec{V}_{\text{p}}, \tag{5}$$

$$\frac{\mathrm{d}\vec{V}_{\text{p}}}{\mathrm{d}t} = \vec{F}_{\text{p}} + \vec{F}, \tag{6}$$

where $\vec{V}_{\text{p}}$ and $\vec{X}_{\text{p}}$ represent the velocity and positional distributions of the particle phase, respectively. $\vec{F}_{\text{p}}$ is the drag force received by the particle population per unit mass, and $\vec{F}$ is the other forms of force on the particles, including Stefan flow, pressure gradient forces, and so on.

The drag force received by the particle population per unit mass is defined as

$$\vec{F}_{\text{p}} = \frac{3}{4} \frac{C_D \rho}{\rho_P d_P} (\vec{V} - \vec{V}_{\text{p}})|\vec{V} - \vec{V}_{\text{p}}|. \tag{7}$$

Here C_D is the resistance coefficient, which can be calculated by the following equation [37]:

$$C_D = \begin{cases} \frac{24}{\text{Re}_p}\left(1 + \frac{1}{6}\text{Re}_p^{2/3}\right), & \text{Re}_p < 1000 \\ 0.44, & \text{Re}_p > 1000 \end{cases}. \tag{8}$$
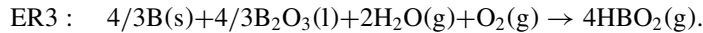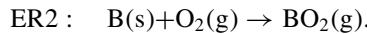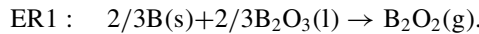
Re_p in the above equation represents the Reynolds number of the particles and is defined as follows:

$$\text{Re}_{\text{p}} = \frac{\rho d_{\text{p}}|\vec{V} - \vec{V}_{\text{p}}|}{\mu}. \tag{9}$$

C. Combustion model

This paper utilizes a simplified seven-step hydrogen combustion reaction mechanism [38,39]. The optimized ignition model of boron particles is selected, where the ignition process is influenced by the oxide layer thickness on the particle surface [40,41].

The ignition process includes the following reactions:

ER1 : $2/3\text{B(s)} + 2/3\text{B}_2\text{O}_3\text{(l)} \rightarrow \text{B}_2\text{O}_2\text{(g)}$.

ER2 : $\text{B(s)} + \text{O}_2\text{(g)} \rightarrow \text{BO}_2\text{(g)}$.

ER3 : $4/3\text{B(s)} + 4/3\text{B}_2\text{O}_3\text{(l)} + 2\text{H}_2\text{O(g)} + \text{O}_2\text{(g)} \rightarrow 4\text{HBO}_2\text{(g)}$.

The ER1 reaction rate is obtained through Eq. (10):

$$R_1 = P^0_{\text{B}_2\text{O}_2}\big/\big(1/\alpha_1 v_1 + 1\big/\big(D_{\text{B}_2\text{O}_2,\text{g}}\text{Nu}/2R u T_p r_p\big)\big),$$

$$\alpha_1 = 0.03,$$

$$v_1 = 6.06 T_p^{-0.5} \ (\text{mol}/(\text{m}^2 - \text{atm} - \text{s})),$$

$$\log P^0_{B_2O_3} = 6.609 - 72400/4.575T_p; \ \text{(atm)}$$

$$D_{B_2O_2,g} = 1.937e^{-5}P^{-1}T_p^{3/2}; \tag{10}$$

Nu, Ru, T_p, and r_p, respectively, represent the Nusselt number, gas constant, particle temperature, and particle radius.

The ER2 reaction rate is obtained through Eq. (11):

$$R_2 = X^0_{BO} / \left(\frac{1}{\alpha_2 v_2 P_{O_2}} + \frac{x}{D_{BO}n} \right)$$

$$X^0_{BO} = 2.32e^{-2}[1 - \exp(35000/T_p - 35000/1300)]$$

$$\alpha_2 = 0.035$$

$$v_2 = 7.84T_p^{-0.5}; \ (\text{mol}/(\text{m}^2 - \text{atm} - \text{s}))$$

$$D_{BO} = 5.11e^{-5}\exp(-7500/T_p); \ (\text{cm}^2/\text{s})$$

$$n = 0.0266; \ (\text{mol}/\text{cm}^3) \tag{11}$$

x represents the thickness of the particle's oxide layer.

The ER3 reaction rate is obtained through Eq. (12):

$$R_3 = X^0_{BO} / \left(\frac{1}{\alpha_3 v_3 P_{H_2O}} + \frac{x}{D_{BO}n} \right)$$

$$\alpha_3 = 0.4\exp(-5500/T_p)$$

$$v_3 = 10.54T_p^{-0.5} \ (\text{mol}/(\text{m}^2 - \text{atm} - \text{s})) \tag{12}$$

The reaction heats of ER1, ER2, and ER3 are Q1, Q2, and Q3, with values of -303.06, 284.64, and 87.90 KJ/mol, "–" indicates the heat absorption of the reaction. The control equation during the ignition process is as follows:

$$\frac{dr_p}{dt} = -\left[\frac{2}{3}R_1 + R_2 + \frac{4}{3}R_3 \right] \frac{M_B}{\rho_B} \tag{13}$$

$$\frac{dx}{dt} = -\left[\frac{2}{3}R_1 + \frac{4}{3}R_3 \right] \frac{M_{B_2O_3}}{\rho_{B_2O_3}} \tag{14}$$

$$\frac{dT_p}{dt} = \frac{4\pi(r_P + x)^2 \left[-\sum_{j=1}^{3} R_j Q_j + h_c(T_\infty - T_p) + \sigma\varepsilon_B(T_\infty^4 - T_p^4) \right]}{\left(\frac{4}{3}\pi r_p^3 \rho_B C_{p,B} + \frac{4}{3}\pi r_p^2 x \rho_{B_2O_3} C_{p,B_2O_3} \right)} \tag{15}$$

In Eqs. (13) and (14), M_B, ρ_B, $M_{B_2O_3}$, and $\rho_{B_2O_3}$ represent the molar mass and density of boron and boron oxide, respectively. In Eq. (15), $h_c(T_\infty - T_p)$ represents convective heat transfer, and $\sigma\varepsilon_B(T_\infty^4 - T_p^4)$ represents radiative heat transfer, and $C_{p,B}$ and C_{p,B_2O_3} represent the specific-heat capacities of boron and boron oxide, respectively. When the oxide film is completely consumed and the oxide film thickness x equals 0, the particle ignition is completed, and the boron particle enters the combustion stage.

During the combustion stage of boron particles, the surface reaction processes between boron, oxygen, and water vapor are mainly considered. The main reaction processes are as follows:

$$\text{ER4}: \quad 2B(s) + O_2(g) \rightarrow B_2O_2(g),$$

$$\text{ER5}: \quad 2B(S) + H_2O(g) + 3/2O_2(g) \rightarrow 2HBO_2(g).$$
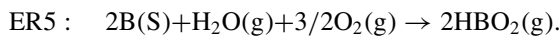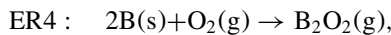
The ER4 reaction rate is obtained through Eq. (16):

$$R_4 = k_{4,s}x_{O_2,\infty}P,$$

$$k_{4,s} = k_{4,\infty}/f_{GR4}; \; (\text{mol}/(\text{cm}^{2*}\text{s}^*\text{atm})),$$

$$K_{4,\infty} = \begin{cases} 0.0625^*1519.77, & T_P > 2400\,\text{K} \\ 1.247 - 2.637e - 4T_P, & 2400\,\text{K} \geqslant T_P > 1750\,\text{K}, \\ -13.14 + 1.795e - 2T_P - 5.716e - 6T_P^2, & 1750\,\text{K} \geqslant T_P > 1600\,\text{K} \end{cases}$$

$$f_{GR4} = \begin{cases} 0.6175, & T_P > 2400\,\text{K} \\ 1.247 - 2.637e - 4T_P, & 2400\,\text{K} \geqslant T_P > 1750\,\text{K}. \\ -13.14 + 1.795e - 2T_P - 5.716e - 6T_P^2, & 1750\,\text{K} \geqslant T_P > 1600\,\text{K} \end{cases} \tag{16}$$

The ER5 reaction rate is obtained through Eq. (17):

$$R_5 = k_{5,s}\frac{x_{H_2O,s}P}{RuT_p} \times 10e^{-4},$$

$$k_{5,s} = 8.57T_P^{0.5}\exp\left(-8.05e^5T_P^{-2} + 1740T_P^{-1} - 1.32\right). \tag{17}$$

The reaction heats of ER4 and ER5 are Q4 and Q5, respectively, with values of 460.44 and 1620.34 KJ/mol.

During the combustion process, the governing equations are as follows:

$$\frac{dr_p}{dt} = -[2R_4 + 2R_5]\frac{M_B}{\rho_B}, \tag{18}$$

$$\frac{dT_p}{dt} = \frac{4\pi r_p^2\left[-\sum_{j=4}^{5} R_j Q_j + h_c(T_\infty - T_p) + \sigma\varepsilon_B\left(T_\infty^4 - T_p^4\right)\right]}{\left(\frac{4}{3}\pi r_p^3\rho_B C_{p,B}\right)}. \tag{19}$$

When the particle radius r_p equals zero, the combustion stage of boron particles ends.

D. Method verification

Detailed calculation conditions and calculation process can be found in Ref. [28]. This paper only shows the verification results of the hydrogen combustion model and the boron particle combustion model in supersonic airflow, as shown in Figs. 1 and 2.

According to the verification calculation results, the numerical calculation results align with the experimental data, displaying a consistent trend and reasonable agreement.

E. Calculation scheme and grid-independent test

The scramjet structure employed in this study is shown as illustrated in Fig. 3. The combustion chamber has a length L of 1600 mm, a height H of 35 mm, and a width D of 40 mm. The double-stage cavity structure is adopted, with an expansion angle of 0.5° between the two cavity stages and an expansion angle of 2° after the second cavity. Hydrogen is injected at 10 mm ahead of the front edge of the two cavities, while boron particles are injected at 50 mm from the front edge of the second cavity. The geometric dimensions of the cavity are illustrated in Fig. 4, where the cavity height h_c is 12 mm, cavity length l_c is 96 mm, the rear edge is inclined at an angle of 135°, and the particle injection expansion angle is θ.

The computational grid is shown in Fig. 5, utilizing a structured grid. The computational boundary conditions are presented in Table I. In the numerical simulations, the inlet of the combustion chamber is specified as a pressure inlet boundary condition, while the outlet is set as a pressure outlet. The surfaces of the combustion chamber walls are assumed to be adiabatic no-slip walls.

The number of grids with different resolutions is presented in Table II, and the influence of grid quantity on calculation accuracy is analyzed by studying the axial distribution of flow-field pressure.
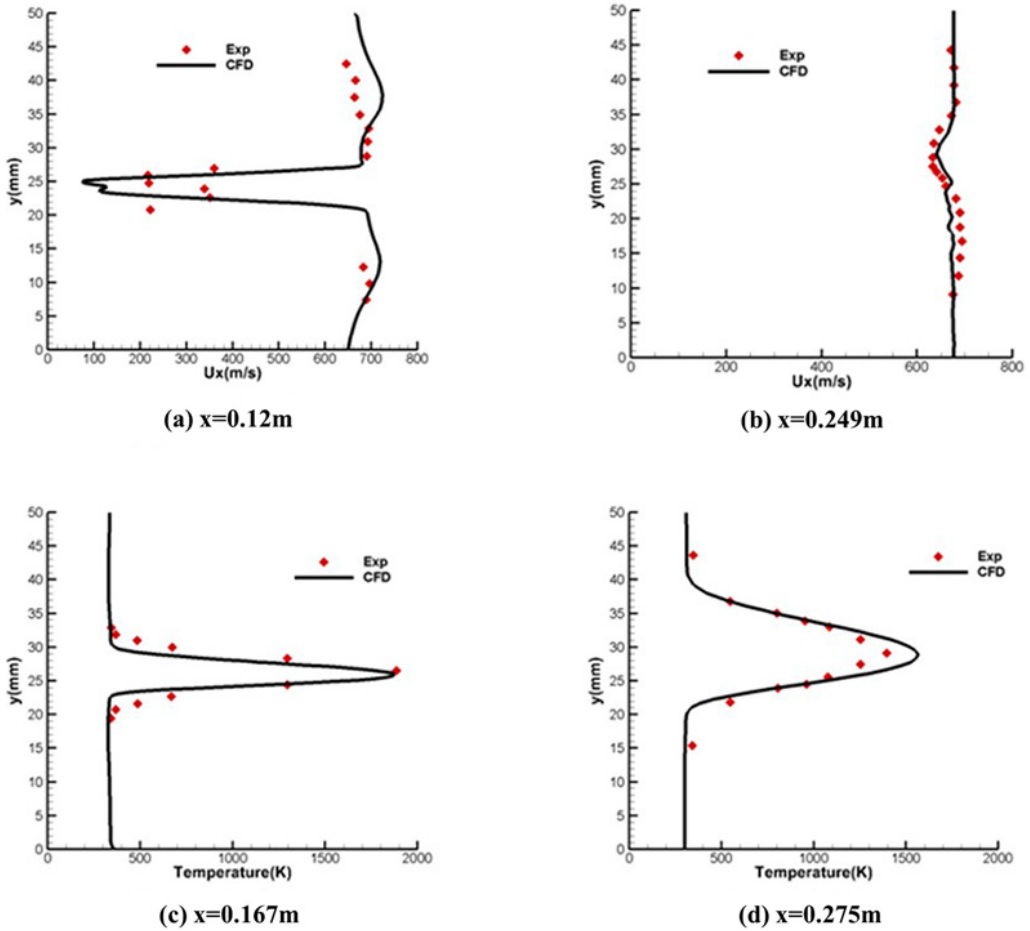
(a) x=0.12m

(b) x=0.249m

(c) x=0.167m

(d) x=0.275m

FIG. 1. Validation of hydrogen combustion model in supersonic airflow.

(a) Cold field combustion chamber
pressure distribution

(b) Combustion chamber pressure
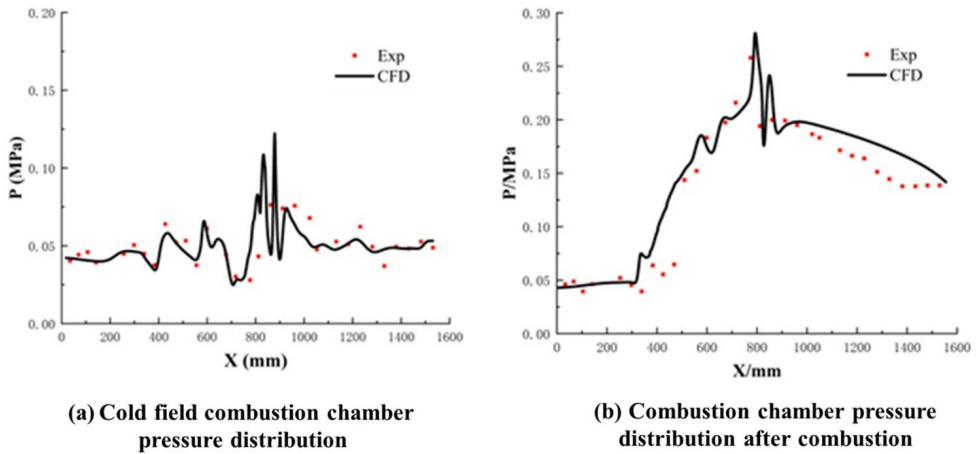distribution after combustion

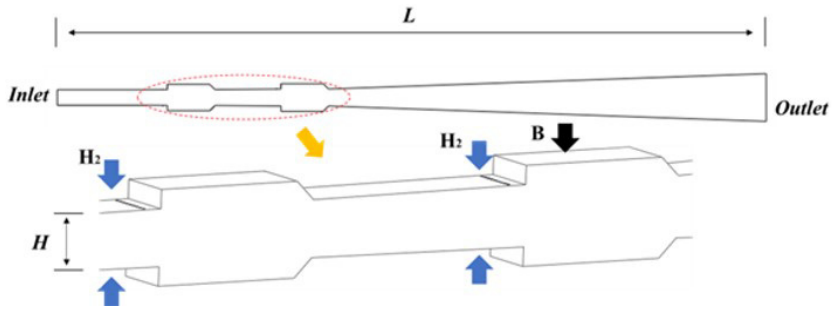FIG. 2. Validation of boron combustion model in supersonic airflow.

FIG. 3. Schematic diagram of combustion chamber structure.

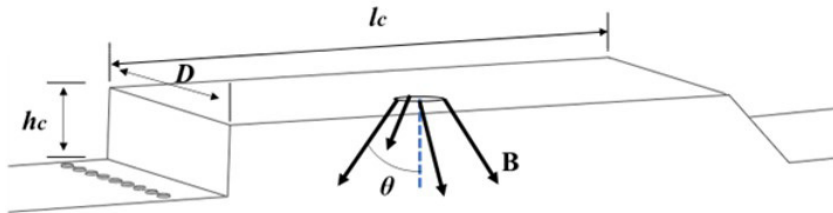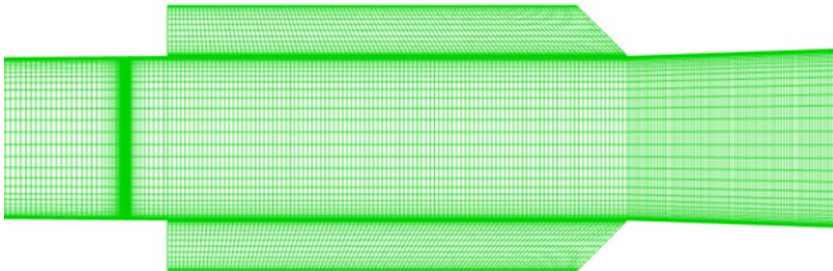FIG. 4. Schematic diagram of cavity.

FIG. 5. Localized schematic of the numerical calculation grid.

TABLE I. Boundary condition.

Parameters	Incoming flow	Powder fuel	Hydrogen
Total temperature (K)	1336	300	300
Total pressure (MPa)	0.797	1.0	1.0
Mass flow (g/s)	460	6	/
Mach number	2.5	/	/

TABLE II. Grid independence analysis.

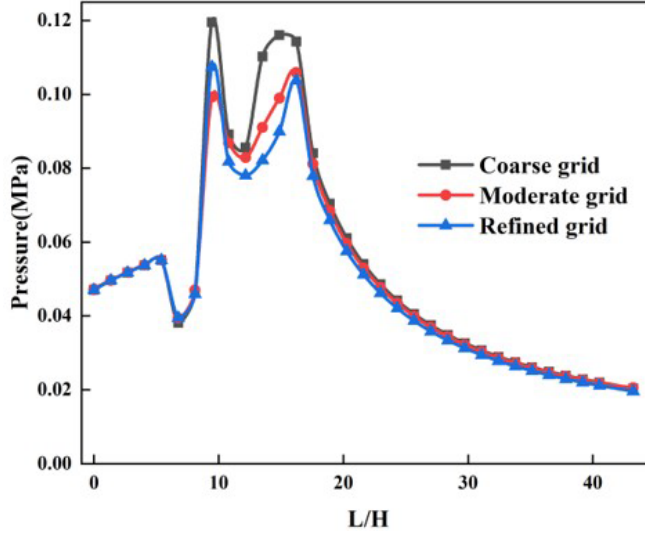| Scale	Number of nodes
Coarse grid	1550000
Moderate grid	2490000
Refined grid	3590000

FIG. 6. Pressure distribution at different cross-sections in the axial direction of the combustion chamber.

Based on the computational results depicted in Fig. 6, it can be observed that the pressure in the flow field of the coarse grid is higher in the cavity region. The pressure distribution between the moderate and refined grids is similar. Taking into account the tradeoff between computational accuracy and cost, this study adopts the moderate grid.

F. Definition of relevant parameters

The swirl degree of the particle injection is defined as a function of the axial velocity $\vec{V}_{\text{axis}}$ and the tangential velocity $\vec{V}_{\text{swirl}}$ using the equation

$$SF = \frac{|\vec{V}_{\text{swirl}}|}{|\vec{V}_{\text{axis}}| + |\vec{V}_{\text{swirl}}|} \tag{20}$$

The combustion efficiencies of boron particles and hydrogen are calculated using the following equation:

$$\eta_s = 1 - \frac{C_{m,\text{residual}}}{C_{m,\text{start}}} \tag{21}$$

where $C_{m,\text{res}}$ represents the mass of the remaining boron particle phase, and $C_{m,\text{sta}}$ is the mass of the initial boron particles,

$$\eta_{i,g} = 1 - \frac{\int \rho u Y_{i,g} dA}{\dot{m}_{i,g} + \dot{m}_{i,\text{new}}} \tag{22}$$

In the above equation $Y_{i,g}$ denotes the hydrogen mass fraction, $\dot{m}_{i,g}$ denotes the total mass flow rate, and $\dot{m}_{i,\text{new}}$ is the mass fraction of the generated gas component.

III. RESULTS AND DISCUSSION

A. The hydrogen/air combustion flame flow field

Before delving into the influence of boron particle injection on the hydrogen flame flow field, an analysis was conducted employing various injection strategies to assess the impact of hydrogen injection at different flow rates at the leading edges of the first- and second-stage cavities. The

TABLE III. The hydrogen/air combustion flame flow field.

Case	First cavity hydrogen injection mass flow rate (g/s)	Second cavity hydrogen injection mass flow rate (g/s)
1	1	0
2	2	0
3	1	1
4	1	2

objective was to optimize the parameters of hydrogen injection, thus laying the groundwork for subsequent research endeavors. Computational conditions are outlined in Table III.

To quantitatively investigate the influence of the injection strategies on the hydrogen flame field, temperature and Mach number distribution curves under different conditions are shown in Figs. 7 and 8. These conditions are distinguished based on the hydrogen injection flow rates before the two-stage cavity. For instance, when the hydrogen injection flow rates before the two-stage cavity are both 1 g/s, the condition is denoted as 1–1.

As shown in Fig. 7, l_1 represents the axial distance of the flow field, higher temperatures are observed within the hydrogen flame field between 250–350 mm (first-stage cavity) and 500–600 mm (second-stage cavity). Notably, at a hydrogen injection flow rate of 2 g/s, the temperature within the field is elevated, up to 2200 K. Furthermore, with both hydrogen injection flow rates set at 1 g/s, the flow-field temperature in the second stage cavity is also higher, exceeding 2000 K.

From Fig. 8, it is evident that there exists a subsonic flow field within the two-stage cavity, resulting in a decrease in Mach number within the cavity-covered flow-field region. The Mach number distribution within the cavity region is relatively uniform, with the Mach number in the second-stage cavity region being lower than that in the first-stage cavity region. The Mach number of the flow field decreases with the increase of the hydrogen jet flow in front of the cavity.

Combustion chamber flow-field temperature and Mach number changes are affected by hydrogen combustion heat release. In the combustion chamber of the two-stage cavity scramjet, the hydrogen combustion efficiency is depicted in Fig. 9. To differentiate between the hydrogen combustion efficiencies within the two-stage cavities under various conditions, the conditions are labeled based
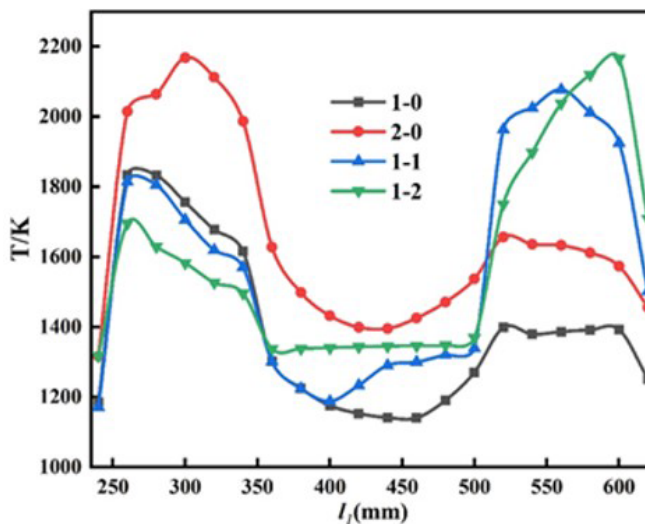

FIG. 7. Temperature distribution curve of flame flow field under different injection strategies.
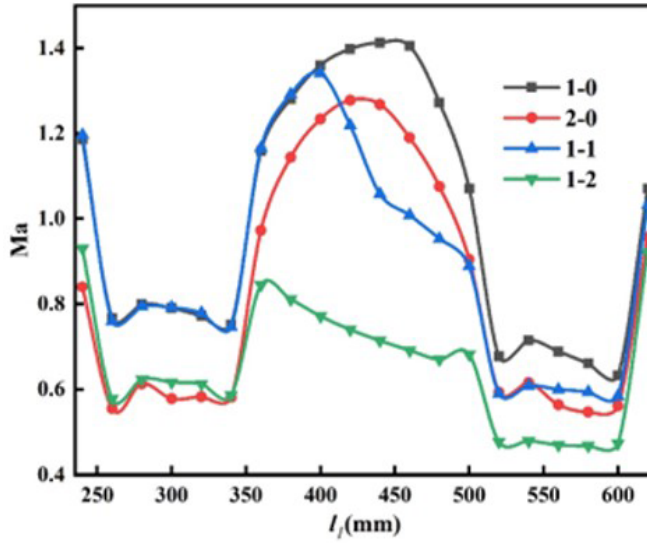
FIG. 8. Mach number distribution curve of flame flow field under different injection strategies.

on the hydrogen injection flow rates at the leading edges of the first- and second-stage cavities. For instance, when hydrogen is injected at 1 g/s into both stages of the cavity, the hydrogen combustion efficiency in the first-stage cavity is denoted as 1–1–1st, whereas in the second stage cavity, it is indicated as 1–1–2nd.

In Fig. 9, hydrogen swiftly undergoes combustion after injection, and l_0 represents the axial distance from the hydrogen injection location to the flow field, with near-complete combustion occurring approximately 100 mm downstream from the injection point, indicating thorough combustion within the cavities. Within the same cavity, an increase in hydrogen flow rate correlates
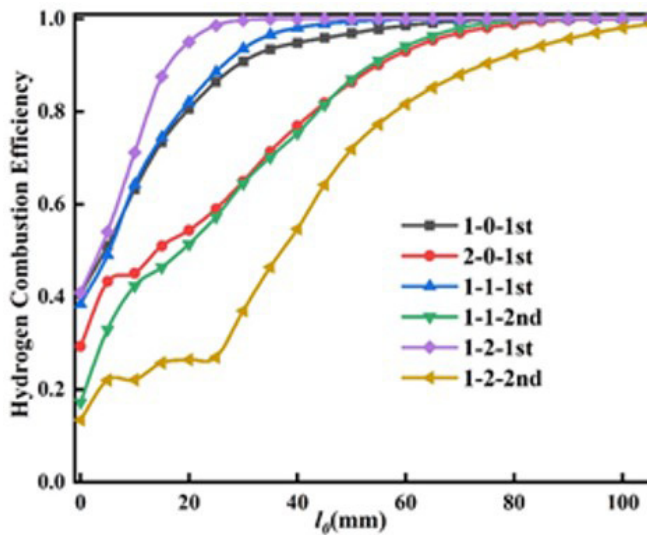

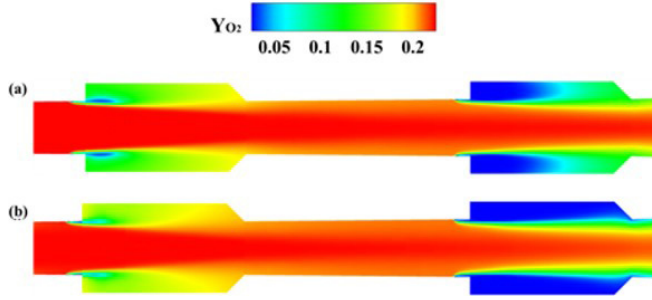FIG. 9. Hydrogen combustion efficiency under different injection strategies.

FIG. 10. O_2 concentration distribution in flame flow field under different injection strategies.

with a decrease in combustion efficiency. When hydrogen injection rates are consistent, higher combustion efficiency is observed in the first-stage cavity (1st) compared to the second-stage (2nd).

Figure 9 also reveals that increasing the hydrogen injection flow rate into the second-stage cavity enhances the combustion efficiency of hydrogen injected before the first-stage cavity. This increase is attributed to a reduction in the heat released from hydrogen combustion entering the cavity flow field, consequently leading to a decrease in the temperature within the cavity region. Conversely, within the second-stage cavity, as the hydrogen injection flow rate before the cavity increases, the temperature of the flame field rises. At a hydrogen injection flow rate of 2 g/s before the cavity, however, the combustion efficiency of hydrogen decreases, resulting in a shift in the location of the temperature peak within the flow field.

Furthermore, as illustrated in Fig. 10, an increase in hydrogen flow rate leads to higher oxygen consumption. For instance, in Case 3 [Fig. 10(a)], hydrogen is injected at 1 g/s in the first-stage cavity, while in Case 4 [Fig. 10(b)], it increases to 2 g/s before the second-stage cavity. This results in a decrease in oxygen concentration within the second-stage cavity, leading to decreased hydrogen combustion efficiency. Additionally, when both cavities receive hydrogen injections at 1 g/s (Case 3), the oxygen concentration within the first-stage cavity surpasses that of the second-stage cavity, contributing to higher combustion efficiency in the former.

In summary, when the hydrogen injection flow rate before the cavity is 2 g/s, the heat release from hydrogen combustion is high, resulting in a significant decrease in flow field Mach number despite the higher flow-field temperature. Only when the hydrogen injection flow rate before the first-stage cavity is 1 g/s is the flow-field Mach number higher, but the heat release of hydrogen is less, leading to a lower flow-field temperature. When the hydrogen injection flow rates before both two-stage cavities are 1 g/s, the flow-field temperature and Mach number are higher in the second-stage cavity, and except for the cavity region, the flow-field Mach number is higher than 1.

Therefore, considering the distribution of hydrogen flame flow-field temperature and Mach number, and due to the relatively uniform Mach number distribution within the cavity region and the lower Mach number near the second-stage cavity, subsequent studies will adopt a hydrogen injection scheme of 1 g/s before both two-stage cavities, with particle injection on the wall of the second-stage cavity, positioned at the center of the cavity, specifically 50 mm from the front edge of the cavity.

B. The influence of particle injection expansion angle

Under the conditions of hydrogen injection rates of 1 g/s in both two-stage cavities, a particle diameter of 5 μm, the injection speed is 100 m/s, and the swirl degree is 0, the influence of particle injection expansion angle on the characteristics of hydrogen flame flow field was studied. The definition of particle injection expansion angle is provided in Sec. II E, and the operating conditions are listed in Table IV.

TABLE IV. The influence of particle injection expansion angle.

Case	Boron particle injection expansion angle
5	0°
6	15°
7	30°
8	45°

As the particle injection expansion angle increases from 0° to 45°, the particle combustion efficiency is illustrated in Fig. 11, and l_2 represents the axial distance from the boron particle injection location to the flow field. At a 0° injection expansion angle, the particles undergo minimal combustion. However, as the particle injection expansion angle increases, the particle combustion efficiency rises, with the highest efficiency reaching 0.65 at a 45° injection expansion angle. Therefore, compared to the computational results in [28], the increase in particle injection diffusion angle to 45° led to a higher rate of increase in particle combustion efficiency, with combustion efficiency exceeding 0.6 at 100 mm from the injection position.

Particle combustion efficiency is related to particle flow time and particle dispersion degree. At different injection expansion angles, the particle flow time is illustrated in Fig. 12. At injection expansion angles of 0° and 15°, the particle flow times are similar. However, as the injection expansion angle increases further to 30° and 45°, the particle flow time increases. Notably, at a 45° injection expansion angle, the particle flow time can reach 0.9 ms.

The combustion efficiency of particles is related to their dispersion and residence time in the flow field. The particle trajectories under injection expansion angles of 15° (a) and 45° (b) are depicted in Fig. 13, revealing a more dispersed particle distribution at a 45° injection expansion angle.

Therefore, because the particle flow time is longer and the particle diffusion is more uniform, the particle combustion efficiency is higher when the particle expansion angle is 45°.

The difference of particle combustion efficiency leads to the difference of combustion chamber temperature distribution under different particle injection expansion angles. The temperature distribution in the flow field under different injection expansion angles is shown in Fig. 14. Compared
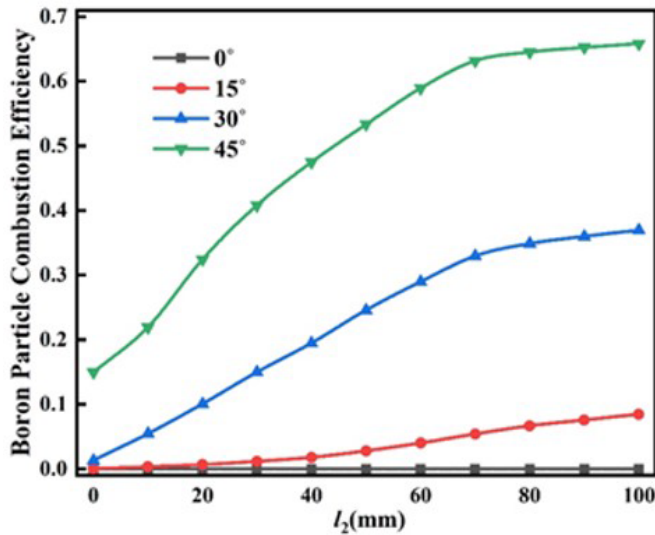

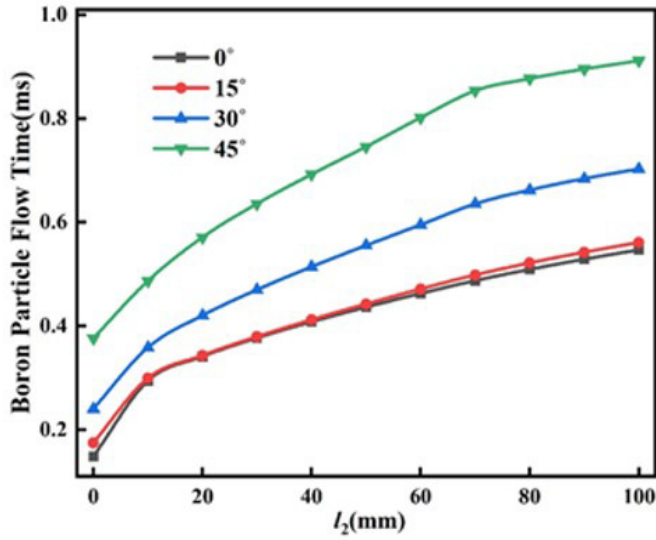FIG. 11. Boron particle combustion efficiency under different injection expansion angles.

FIG. 12. Boron particle flow time under different injection expansion angles.

with the flow-field temperature before particle injection, the flow-field temperature drops after particle injection. When the particle injection expansion angle is 0°–30°, the flow-field temperature is always lower than that before particle injection. When the particle injection expansion angle reaches 45°, the flow-field temperature drops significantly after particle injection and then increases gradually, and the temperature of the flow field behind the injection position is higher than that before the injection, as shown in Fig. 15.

As shown in formulas (12) and (16), particle temperature during ignition combustion is affected by combustion reaction heat, flow-field convection, and radiation heat transfer. When particle temperature is lower than flow-field temperature, if combustion reaction heat release or combustion reaction heat absorption (such as ER1) is insufficient, particles will absorb heat from the flow field through convection and radiation heat transfer; when particle temperature is higher than flow-field temperature, the particles will release heat into the flow field.
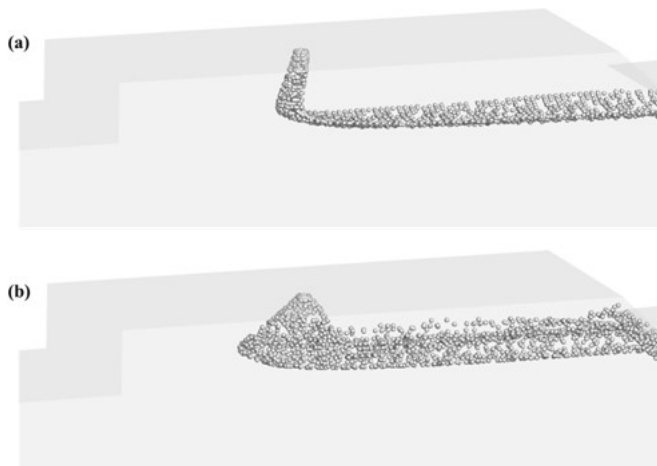

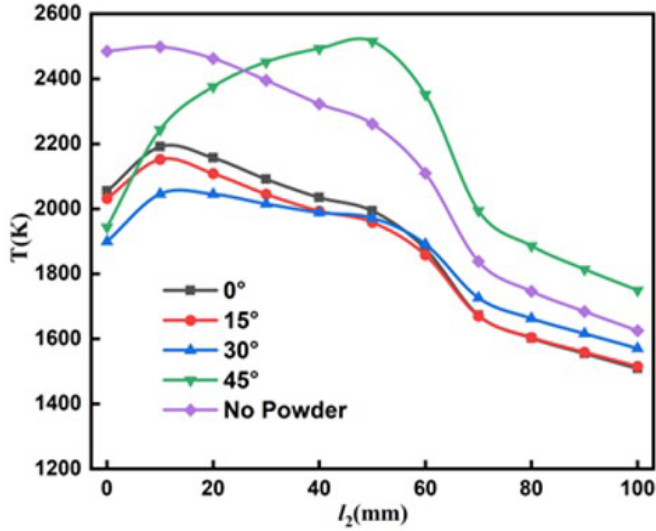FIG. 13. The particle trajectories under different injection expansion angles.

FIG. 14. Temperature distribution curve under different injection expansion angles.

The particle heat absorption Q1 under different injection expansion angles is shown in Fig. 16. The heat absorption of particles is calculated based on the specific heat of the particles and the change in particle mass and temperature. When Q1 is greater than 0, it indicates that the particles are absorbing heat as they warm up. When Q1 is less than 0, it indicates that the particles are releasing heat as they cool down. Figure 17 shows the combustion heat Q2 of particles under different injection expansion angles. When Q2 is greater than 0, it indicates that the particles absorb the heat of combustion; when Q2 is less than 0, it indicates that the reaction absorbs particle heat. Moreover, as the particle radius decreases, according to Eqs. (15) and (19), this leads to fluctuations in particle combustion heat Q2.

As the particle injection expansion angle increases from 0° to 30°, according to Fig. 16, particles absorb a lot of heat at the injection position ($l_2 = 0$ mm), while Fig. 17 shows that at the injection position ($l_2 = 0$ mm), particles hardly release heat from combustion. When the injection angle reaches 45°, although the heat release from the combustion reaction is higher at the injection position
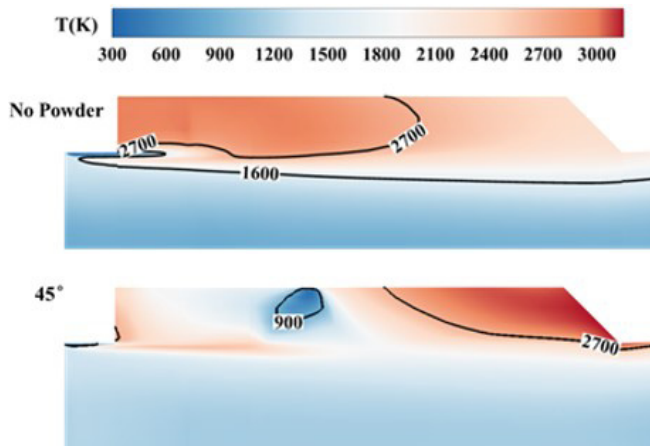

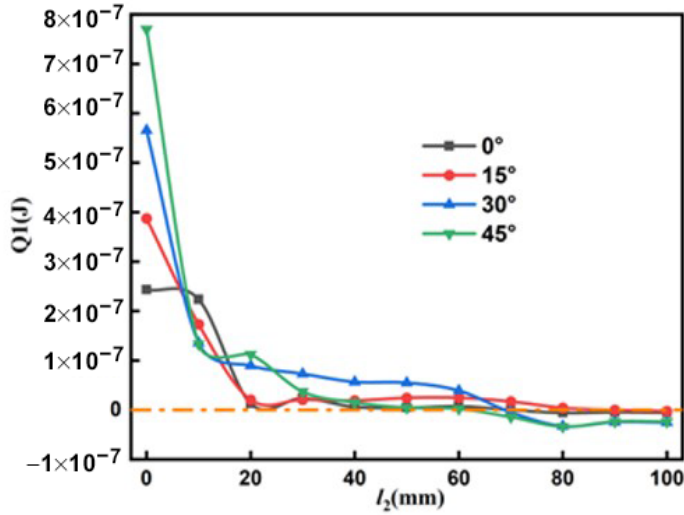FIG. 15. Temperature distribution under different injection expansion angles.

FIG. 16. Particle heat absorption under different injection expansion angles.

($l_2 = 0$ mm), the combustion heat is less than the heat absorption of particles, which indicates that particles absorb heat from the flow field to meet the needs of particle heating, leading to a decrease in the temperature of the flow field.

When the particle injection expansion angle is 45°, in the region downstream of the particle injection point ($l_2 = 30$ mm), the heat absorption Q1 by the particles is close to zero. Subsequently, at $l_2 = 70$ mm, Q1 becomes less than 0. At the same time, Q2 is always greater than 0, which leads to the particles releasing heat to the flow field at this injection expansion angle, resulting in an increase in the flow-field temperature.

In summary, with an increase in the injection expansion angle of particles, the particle combustion efficiency improves. However, the influence of particle combustion efficiency on the flow-field
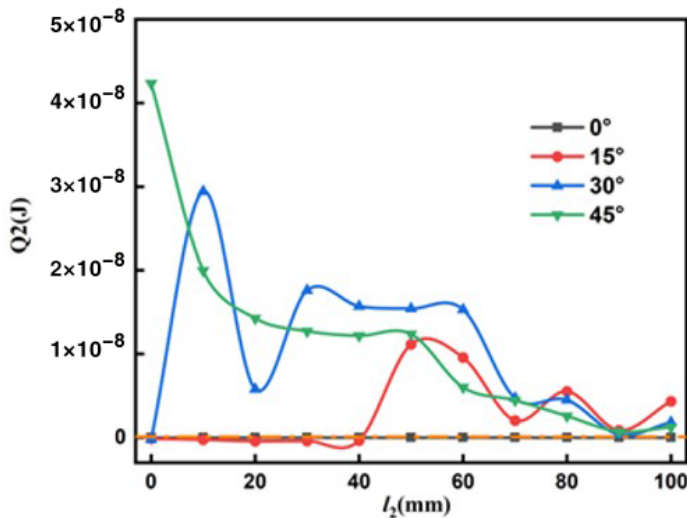

FIG. 17. Heat of particle combustion under different injection expansion angles.

TABLE V. The influence of swirl degree.

Case	Boron particle injection swirl degree
9	0
10	0.2
11	0.3
12	0.4

temperature is nonlinear. Only when the injection expansion angle reaches 45°, at the back of the injection position, is the temperature of the flow field higher than that before the particle injection.

C. The influence of swirl degree

Examine the impact of particle injection swirl on the hydrogen flame flow field within the supersonic combustion chamber, under the conditions of an injection velocity of 100 m/s, a particle diameter of 5 μm, and an injection expansion angle of 0°. The operational parameters are presented in Table V.

As shown in Fig. 18, when the particle injection swirl increases from 0 to 0.4, the particle combustion efficiency rises. At a swirl of 0, particles undergo minimal combustion, but as the swirl increases, particle combustion efficiency improves. Notably, at a swirl of 0.4, the particle combustion efficiency peaks at 0.39.

Figure 19 depicts the particle flow time under different swirl conditions. Similar particle flow times are observed at swirls of 0 and 0.2. However, as the swirl increases to 0.3 and 0.4, the particle flow time increases. Notably, at a swirl of 0.4, the particle flow time can reach up to 0.7 ms.

Figure 20 illustrates the particle trajectories under swirl conditions of 0.2 (a) and 0.4 (b), revealing a more dispersed particle distribution at a swirl of 0.4. Comparing with the computational results in [28], swirl injection of particles can also increase the rate of increase in particle combustion efficiency.
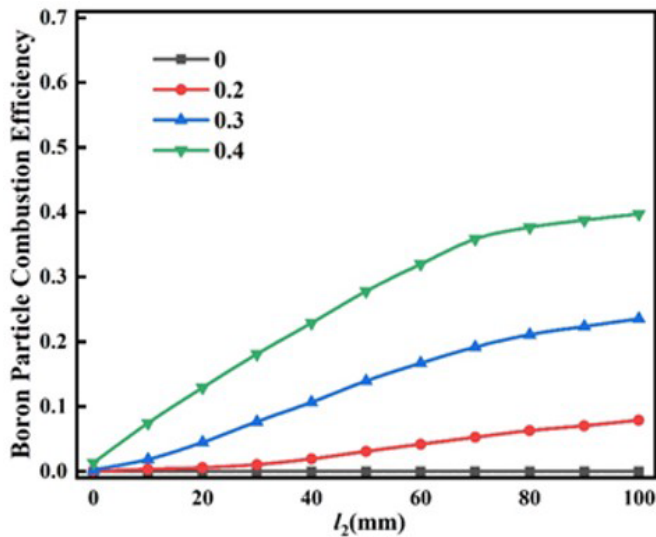

FIG. 18. Boron particle combustion efficiency under different injection swirl degrees.
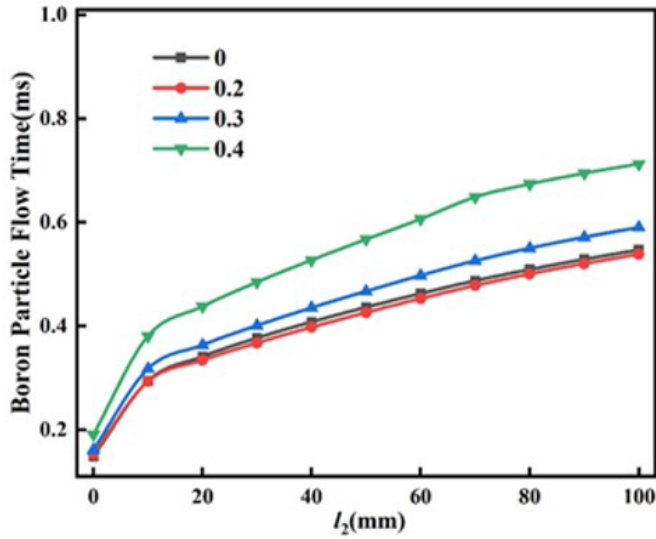
FIG. 19. Boron particle flow time under different injection swirl degrees.

Therefore, the improved particle dispersion and longer residence time at a swirl of 0.4 results in a higher particle combustion efficiency at this injection swirl degree.

The temperature distribution under different injection swirl conditions is illustrated in Fig. 21. When the swirl degree goes from 0 to 0.3, the flow-field temperature is lower than before particle injection. When the swirl degree reaches 0.4, the overall flow field temperature is lower, with only the flow-field temperature behind the injection position approaching the temperature before particle injection, as illustrated in the flow-field temperature contour plot in Fig. 22.

Figures 23 and 24, respectively, depict the heat absorption of particles Q1 and the combustion heat of particles Q2 under different swirl degrees. Due to the more uniform distribution of particles in the flow field at a swirl degree of 0.4, more heat is absorbed by the particles at the injection position ($l_2 = 0$ mm), and because of the shortened particle radius, the combustion heat of the particles also fluctuates.
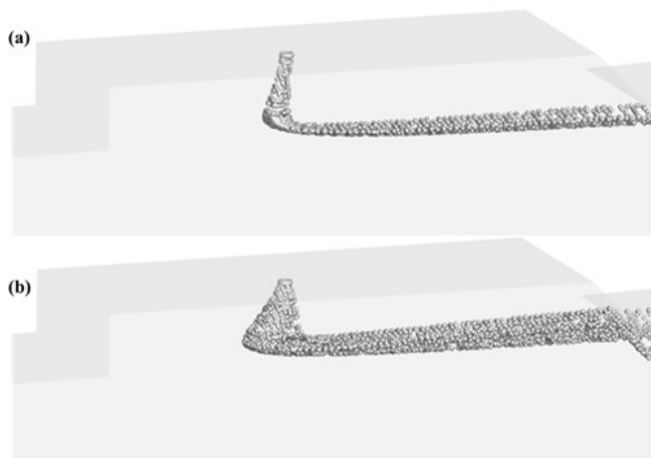

FIG. 20. The particle trajectories under different injection swirl degrees.
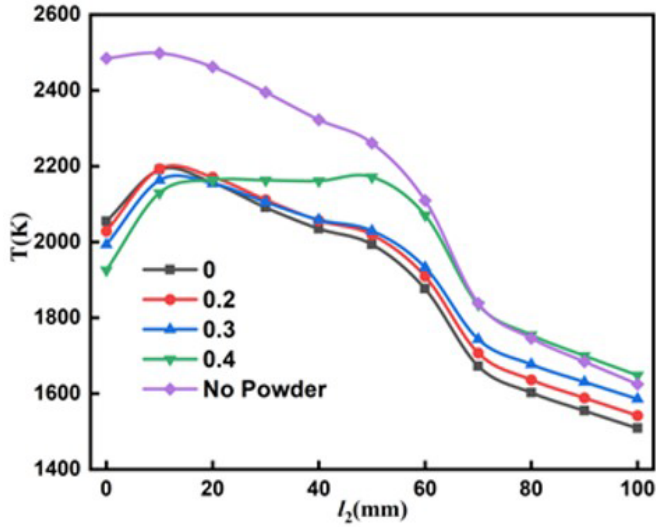
FIG. 21. Temperature distribution curve under different injection swirl degrees.

Comparing with Figs. 16 and 17, the heat absorption of particles is similar, but the combustion heat of particles is lower, and the location where particles release heat is further away from the injection position. The combustion heat of particles cannot meet the heating needs of the particles, causing the particles to need to absorb heat from the flow field, resulting in the overall flow-field temperature being lower than before particle injection. When the swirl degree is 0.4, the particles release heat at $l_2 = 70$ mm, leading to the flow-field temperature approaching the temperature before particle injection.

Summarizing the above findings, although the combustion efficiency of boron particles increases as the particle injection swirl increases from 0 to 0.4, reaching a maximum efficiency of 0.39, due to the lower combustion heat of particles and the release of heat occurring further away from the injection position, particles need to absorb heat from the flow field to meet their heating requirements. It is only when the swirl number reaches 0.4 that the flow-field temperature behind the injection position approaches the temperature before particle injection.
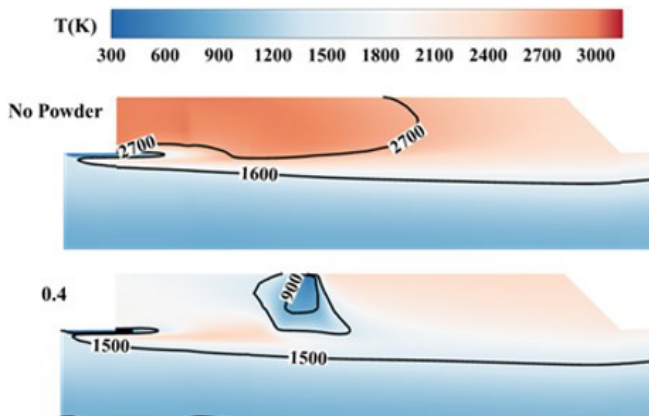

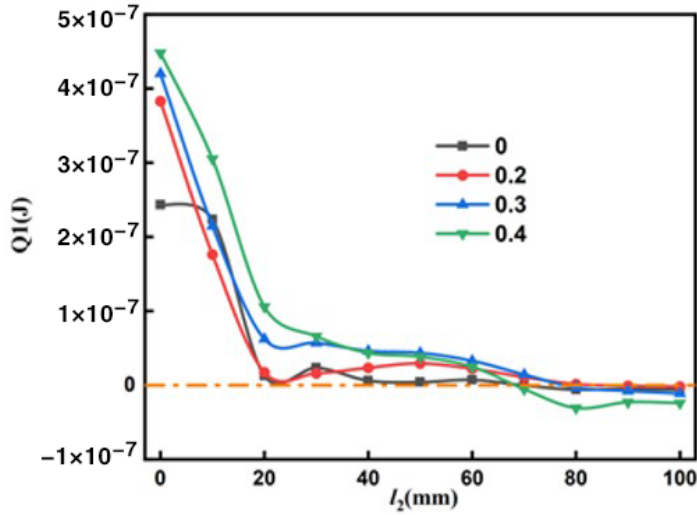FIG. 22. Temperature distribution under different injection swirl degrees.

FIG. 23. Particle heat absorption under different injection swirl degrees.

IV. CONCLUSIONS

This study investigates the influence of hydrogen injection flow rate on the parameters of the hydrogen flame flow field, and it explores the variations in flame flow-field parameters after injecting boron particles into the hydrogen flame flow field. Based on the numerical simulation results, the following conclusions are drawn:

In the hydrogen flame flow field of a two-stage cavity scramjet, the hydrogen combustion efficiency is higher in the first-stage cavity. With an increase in hydrogen injection flow rate in the second-stage cavity, the hydrogen combustion efficiency in the first-stage cavity improves. The temperatures in the two-stage cavities are higher, but the Mach numbers of the flow field are lower. Higher hydrogen injection flow rates result in higher temperatures and lower Mach numbers in the cavities.
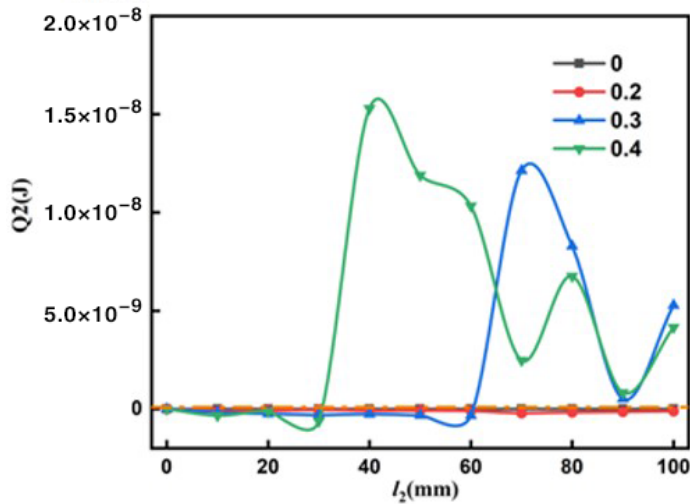

FIG. 24. Heat of particle combustion under different injection swirl degrees.

Comparing with the computational results in [28], expanding the particle injection expansion angle and increasing the particle injection swirl can enhance the combustion efficiency of boron particles. However, due to the comparatively smaller combustion heat of particles compared to their heat absorption, particles absorb heat from the flow field to meet their heating requirements, causing a decrease in flow-field temperature.

---

[1] D. Passiatore, L. Sciacovelli, P. Cinnella, and G. Pascazio, Shock impingement on a transitional hypersonic high-enthalpy boundary layer, Phys. Rev. Fluids **8**, 044601 (2023).

[2] T. Hiejima, Effects of streamwise vortex breakdown on supersonic combustion, Phys. Rev. E **93**, 043115 (2016).

[3] G. Choubey, D. Yuvarajan, W. Huang, Li Yan, H. Babazadeh, and K. M. Pandey, Hydrogen fuel in scramjets-a brief review, Int. J. Hydrogen Energy **45**, 16799 (2020).

[4] G. Saccone, P. Natale, L. Cutrone, and M. Marini, Hydrogen/Air supersonic combustion modelling and validation for scramjet applications, Journal of Fluid Flow **9**, 136 (2022).

[5] C. Cao, T. Ye, and M. Zhao, Large eddy simulation of hydrogen/air scramjet combustion using tabulated thermo-chemistry approach, Chin. J. Aeronaut. **28**, 1316 (2015).

[6] O. R. Kummitha, K. M. Pandey, and A. K. R. Padidam, Effect of a revolved wedge strut induced mixing enhancement for a hydrogen fueled scramjet combustor, Int. J. Hydrogen Energy **46**, 13340 (2021).

[7] S. Wang, Z. Du, W. Huang, and G. Choubey, Numerical study on a novel device for hydrogen mixing enhancement in a scramjet: Coaxial injector, Aerosp. Sci. Technol. **127**, 107680 (2022).

[8] G. Choubey and K. M. Pandey, Effect of different wall injection schemes on the flow-field of hydrogen fuelled strut-based scramjet combustor, Acta Astronaut. **145**, 93 (2018).

[9] T. Hiejima, Theoretical analysis of streamwise vortex circulation induced by a strut injector, Phys. Rev. Fluids **1**, 054501 (2016).

[10] G. Choubey, K. M. Pandey, D. Sharma, and A. Debbarma, Computational simulation of multi-strut central lobed injection of hydrogen in a scramjet combustor, Perspect. Sci. **8**, 222 (2016).

[11] Z. Li, N. H. Abu-Hamdeh, R. A. R. Bantan, and A. Musa, Effects of downstream ramp on the fuel diffusion of single cross jet at supersonic flow: Computational study, Int. J. Heat Mass Transfer **195**, 123183 (2022).

[12] Z. Li, N. H. Abu-Hamdeh, A. Musa, and Y. Zhang, Influence of downstream ramp on mass diffusion of various coaxial hydrogen and air injectors at supersonic combustion chamber, Int. J. Heat Mass Transfer **199**, 123460 (2022).

[13] A. A. Athithan, S. Jeyakumar, and R. Sivakumar, The effect of ramp location in a strut based scramjet combustor under non reacting flow field, IOP Conf. Ser.: Mater. Sci. Eng. **1128**, 012006 (2021).

[14] H. Sitaraman, N. Brunhart-Lupo, M. H. de Frahan, S. Yellapantula, B. Perry, J. Rood, R. Grout, M. Day, R. Binyahib, and K. Gruchalla, Visualizations of direct fuel injection effects in a supersonic cavity flameholder, Phys. Rev. Fluids **6**, 110504 (2021).

[15] W. O. Landsberg, D. Curran, and A. Veeraragavan, Experimental flameholding performance of a scramjet cavity with an inclined front wall, Aerosp. Sci. Technol. **126**, 107622 (2022).

[16] D. Jian and Y. Yude, Effect of non-uniform incoming flow on the mixing enhancement in a scramjet cavity combustor, Int. J. Hydrogen Energy **50**, 758 (2024).

[17] Z. Wang, H. Wang, and M. Sun, Review of cavity-stabilized combustion for scramjet applications, Proc. Inst. Mech. Eng. Part G J. Aerosp. Eng. **228**, 2718 (2014).

[18] T. Roos, A. Pudsey, M. Bricalli, and H. Ogawa, Cavity enhanced jet interactions in a scramjet combustor, Acta Astronaut. **157**, 162 (2019).

[19] Z. Li, T. D. Manh, M. B. Gerdroodbary, N. Dang Nam, R. Moradi, and H. Babazadeh, Computational investigation of multi-cavity fuel injection on hydrogen mixing at supersonic combustion chamber, Int. J. Hydrogen Energy **45**, 9077 (2020).

[20] Z. Wu, Q. Zhang, F. Yu, W. Luo, Z. Gao, and L. Yue, Coupling effect of multicavity on flame stabilization mode transitions in scramjet combustor, J. Propul. Power **39**, 602 (2023).

[21] L. Suneetha, P. Randive, and K. M. Pandey, Numerical investigation on implication of dual cavity on combustion characteristics in strut based scramjet combustor, Int. J. Hydrogen Energy **44**, 32080 (2019).

[22] R. Deng, Y. Jin, and H. D. Kim, Numerical simulation of the unstart process of dual-mode scramjet, Int. J. Heat Mass Transfer **105**, 394 (2017).

[23] A. C. Rajesh, S. Jeyakumar, K. Jayaraman, M. Karaca, and A. A. Athithan, The implications of dual cavity location in a strut-mounted scramjet combustor, Int. Commun. Heat Mass Transfer **145**, 106855 (2023).

[24] H. Ding, C. Zhuo, X. Chen, and H.-y. Deng, Numerical study on powder fuel injection characteristics of powder fuel scramjet, Powder Technol. **399**, 117169 (2022).

[25] S. M. Flesberg, R. Taghavi, and S. Farokhi, Mixing enhancement in a scramjet combustor using fuel jet injection swirl, *22nd AIAA International Space Planes and Hypersonics Systems and Technologies Conference* (AIAA, Orlando, FL, 2018).

[26] J. A. Ahumada Lazo, M. De La Torre Terrazas, R.-H. Chen, and F. Shu, Experimental study of an underexpanded supersonic jet under non-swirling and swirling conditions, *AIAA Aerospace Sciences Meeting* (AIAA, Kissimmee, Florida, 2018).

[27] H. Ding, C. Zhuo, X. Chen, H. Deng, M. Li, B. Sun, and C. Li, Numerical study on the transverse jet flow and mixing characteristics of hydrogen/metal powder fuel in powder fuel scramjet, Fuel **326**, 125088 (2022).

[28] W. Han, C. Hu, J. Li, J. Yang, R. Wei, R. Lei, and C. Li, Numerical investigation on the combustion characteristics of boron powder fuel under H_2/Air flame in a supersonic cavity-based combustor, Int. J. Hydrogen Energy **53**, 343 (2024).

[29] T. Liu, X. Chen, and A. J. Han, Coatings of activated metal hydride and application in the fuel-rich propellant, Chin. J. Energ. Mater. **24**, 868 (2016).

[30] Y. F. Cheng, H. B. Wu, R. Liu, R. Liu, Y.-L. Yao, J. Su, W.-T. Wang, C.-M. and J. Shu, Combustion behaviors and explosibility of suspended metal hydride TiH_2 dust, Int. J. Hydrogen Energy **45**, 12216 (2020).

[31] Y. Li, C. Hu, and X. Zhu, Experimental study on combustion characteristics of powder magnesium and carbon dioxide in rocket engine, Acta Astronaut. **155**, 334 (2019).

[32] Y. Jin, X. Xu, Q. Yang, S. Dou, X. Wang, Q. Fu, and L. Pan, Combustion behavior of hydrocarbon/boron gel-fueled scramjet, AIAA J. **60**, 3834 (2022).

[33] F. R. Menter, Two-equation eddy-viscosity turbulence models for engineering applications, AIAA J. **32**, 1598 (1994).

[34] M. Ou, L. Yan, W. Huang, S. B. Li, and L. Q. Li, Detailed parametric investigations on drag and heat flux reduction induced by a combinational spike and opposing jet concept in hypersonic flows, Int. J. Heat Mass Transf. **126**, 10 (2018).

[35] W. Huang, Effect of jet-to-crossflow pressure ratio arrangement on turbulent mixing in a flowpath with square staged injectors, Fuel **144**, 164 (2015).

[36] W. Xiao, T. Jin, K. Luo, Q. Dai, and J. Fan, Eulerian-Lagrangian direct numerical simulation of preferential accumulation of inertial particles in a compressible turbulent boundary layer, J. Fluid Mech. **903**, A19 (2020).

[37] X. J. Wu and Z. J. Wei, Analysis of the characteristics of scramjet mode and ramjet mode of axisymmetricdual-combustion ramjet, Acta Astronaut. **203**, 125 (2023).

[38] H. Wei and Y. Li, Numerical investigation on the ram–scram transition mechanism in a strut-based dual-mode scramjet combustor, Int. J. Hydrogen Energy **41**, 4799 (2016).

[39] Z. Cai, Z. G. Wang, and M. B. Sun, Effect of combustor geometry and fuel injection scheme on the combustion process in a supersonic flow, Acta Astronaut. **129**, 44 (2016).

[40] X. Hu, Y. H. Xu, W. Ao, Z. X. Zeng, C. B. Hu, and X. F. Zhu, Ignition model of boron particle based on the change of oxide layer structure, Proc. Combust. Inst. **37**, 3033 (2019).

[41] H. Y. Wang, Y. H. Xu, X. Hu, and Z. X. Zeng, Research on the characteristic of secondary combustion of boron-based ducted rocket with swirling air injection, Acta Armamentarii **36**, 619 (2015).